The Egyptian Journal of Remote Sensing and Space Sciences 25 (2022) 765–778

HOSTED BY

Contents lists available at ScienceDirect

The Egyptian Journal of Remote Sensing and Space Sciences

journal homepage: www.sciencedirect.com

Research Paper

Multi-criteria ground water potentiality mapping utilizing remote sensing and geophysical data: A case study within Sinai Peninsula, Egypt

Ali Shebl [a,b,*], Mahmoud Ibrahim Abdelaziz [c,d], Hosni Ghazala [d], Sultan Awad Sultan Araffa [e], Mahmoud Abdellatif [c,f], Árpád Csámer [a]

[a] Department of Mineralogy and Geology, University of Debrecen, 4032 Debrecen, Hungary
[b] Department of Geology, Tanta University, 31527 Tanta, Egypt
[c] Department of Geophysics, University of Miskolc, 3515 Miskolc, Hungary
[d] Department of Geology, Mansoura University, 35516 Mansoura, Egypt
[e] National Research Institute of Astronomy and Geophysics (NRIAG) 11722, Helwan City, Cairo, Egypt
[f] Department of Geology, South Valley University, 83523 Qena, Egypt

ARTICLE INFO

Article history:
Received 8 February 2022
Revised 4 July 2022
Accepted 4 July 2022

Keywords:
Ground water prospecting
Analytic hierarchy process
Sentinel 2
Geoelectric data

ABSTRACT

Groundwater demand has dramatically increased due to the swift demographic explosion, especially in arid areas, where groundwater is considered the main source for all purposes. Thus, this research integrates climatological, lithological, structural, topographical, hydro-morphological, and geoelectrical data to explore groundwater potential zones in the central part of Sinai Peninsula, Egypt using the GIS-based Analytic Hierarchy Process (AHP). Seven thematic layers of soil moisture, rainfall, normalized difference vegetation index, drainage density, lineament density, slope, and land use/land cover were built from different remote sensing data sets. The eighth layer represents a high-resolution lithological map of the study area, constructed utilizing the power of the support vector machine over Sentinel 2 data and accurately assessed with a previously published geological map. Ground Water Potentiality Map (GWPM) was constructed and highlighted four main areas as promising zones. Comprehensive geoelectrical analysis was executed through seventeen deep vertical electrical soundings (VESs) using Schlumberger configuration, isoresistivity mapping, and geoelectric cross-sections along five different profiles. 3D view of the studied area's subsurface geological and structural pattern with groundwater flow direction specification, and adequate aquifer characterization, revealed four main geoelectrical units. Geoelectrical data results reasonably coincided with remote sensing data findings in highlighting three freshwater potential zones. Furthermore, the study strongly recommends integrating low-cost remote sensing datasets in narrowing the zone to be intensively investigated using further costly geophysical approaches or drilling test boreholes.

1. Introduction

Groundwater is the vital source for drinking, irrigation, and enhancing all socio-economic aspects in arid and semi-arid regions (Mukherjee et al., 2012; Todd and Mays, 2004). Egypt in general, and particularly the Peninsula suffers from freshwater deficiency (Araffa et al., 2015; Sultan et al., 2009); besides, the unmanaged population growth takes this issue to the worst. Solving this problem requires a comprehensive exploration program to allocate potential groundwater zones besides a managed plan to monitor and regulate the random exploitation of known groundwater aquifers.

Lately, remote sensing (RS) data not only proved their efficiency in identifying potential groundwater zones (Arnous et al., 2020; Daniel Hervé et al., 2021; El-Rayes et al., 2020; Melese and Belay, 2021) but also transcends in monitoring its deterioration (Arnous and El-Rayes, 2013; Elbeih et al., 2021) and assessing the risk of its invasion by seawater (Fehri, 2021). Integrated geospatial techniques globally help in delineating the groundwater potential zones (Arunbose et al., 2021; Das and Pardeshi, 2018; Qadir et al., 2020), utilizing various multi-criteria decision-making methods e.g. regression models (Ozdemir, 2011), frequency ratio (FR) (Naghibi et al., 2015), influencing factor (IF) (Das and Pardeshi, 2018) and Analytic Hierarchy Process (AHP)(Kumar et al., 2022).

* Corresponding author at: Department of Mineralogy and Geology, University of Debrecen, 4032 Debrecen, Hungary.
E-mail address: ali.shebl@tanta.science.edu.eg (A. Shebl).

https://doi.org/10.1016/j.ejrs.2022.07.002
1110-9823/

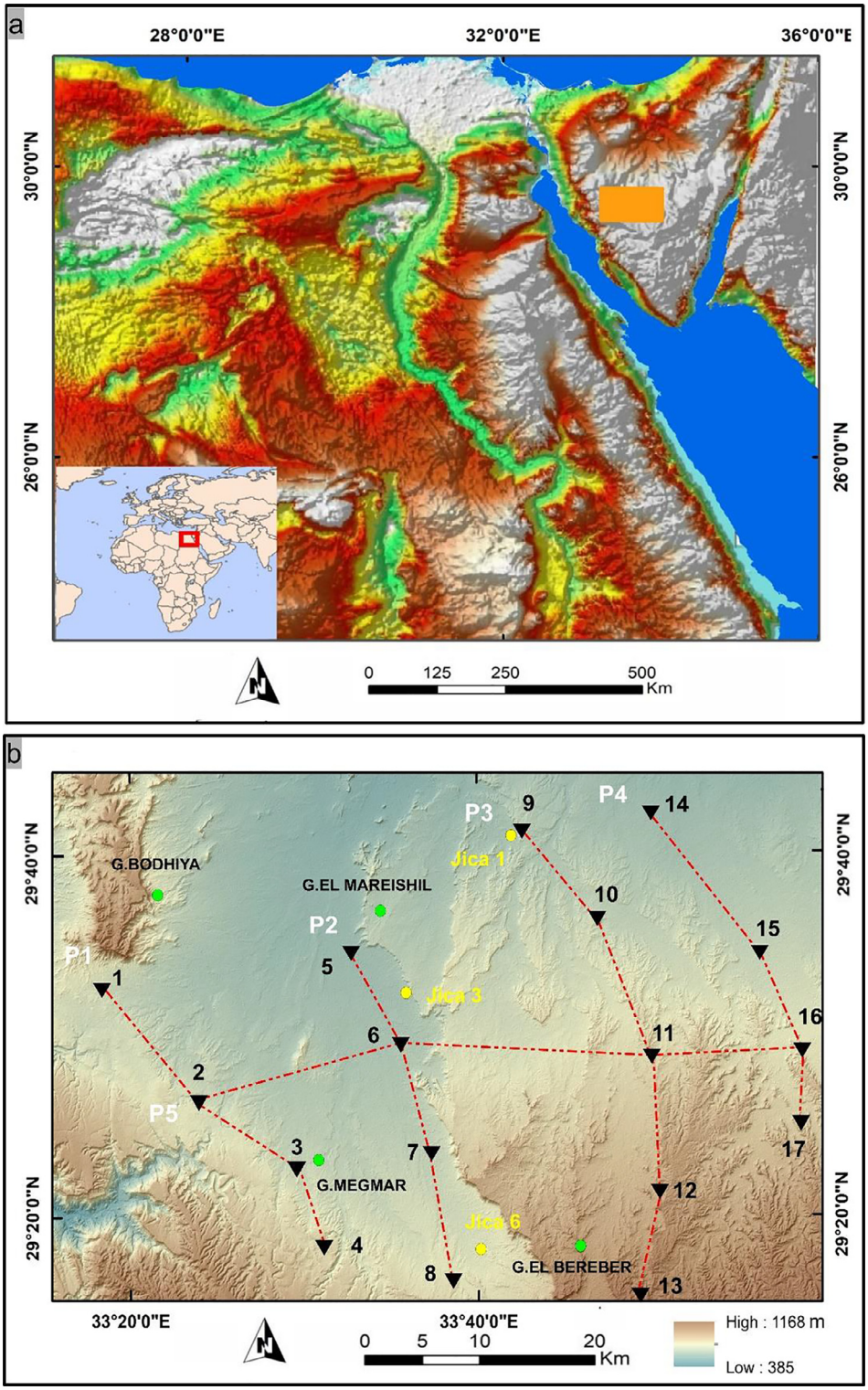

Fig. 1. a) Location map of the study area. b) Location map of the vertical electrical soundings and Jica boreholes in the study area over DEM.

As a structured analysis for interrelated parameters, AHP is widely applied for various water management studies (Arunbose et al., 2021; Abu El-Magd and Eldosouky, 2021). Thus, this research utilized various remote sensing data sets in a comprehensive evaluation of the surface conditions related to groundwater infiltration to highlight zones assumed to be favorable for groundwater storage via multi-criteria overlay analysis using GIS-based AHP. However, the undenied role of remote sensing and GIS based on AHP in solving groundwater potentiality problems (Nigussie et al., 2019), their findings are strongly recommended to be integrated with geophysical tools. Consequently, supplementing AHP results with a geophysical validation highly increased the accuracy of the outputs (Arunbose et al., 2021; Kulandaisamy et al., 2020) and could help decision-makers in executing actual steps for groundwater extraction. The electrical resistivity approach as one of the most often utilized and effective geophysical tools for groundwater

explorations (Lee et al., 2021; Mohamaden and Ehab, 2019; Riwayat et al., 2018) is applied in the current research.

Over different parts of Sinai, several studies (Elbarbary et al., 2021; Elewa and Qaddah, 2011; Mills and Shata, 2009) have implemented GIS and RS data for groundwater potentiality mapping, others (Sultan et al., 2009; Zarif et al., 2021) applied various geophysical measurements for groundwater exploration but the integrated with RS data are not common. Thus, the main aim of the current study is to prospect groundwater in the study area using integrated RS and geoelectrical data. Moreover, Sentinel 2, Phased Array type L band (1.27 GHz) Synthetic Aperture Radar (PALSAR) DEM, Soil Moisture Active Passive (SMAP)/Sentinel-1 L2_SM_SP product, Global Land Cover Map (GLCM) released by Esri, rainfall data, and updated lithological map, were also integrated with geoelectrical data to reveal the main geoelectrical units and assign the fresh groundwater promising zones.

2. Study area and geological setting

The investigated area is located at the western central part of Sinai between latitudes 29° 16″ to 29° 41″ N and longitudes 33° 16″ to 34° 00″ E as shown in Fig. 1a, and occupies an area of about 3700 Km^2. Fig. 1b shows the distribution of seventeen deep vertical electrical soundings (VESs) over the study area. According to UNESCO Cairo Office (2005), the study area is covered by sedimentary rock units, such as Egma, (Lower Eocene chalky limestone), Esna (Paleocene shale), and Sudr Formation (Upper Cretaceous white to pale grey chalk), however, additional stratigraphical units such as Malha, Raha, Wata, Matalla, and Duwi Formation, as well as alluvial hamadah, and quaternary wadi deposits are also represented. As the UNESCO Cairo Office map has a smaller mapping scale (1:500.000) which may cause inconveniences in the current study, special importance was given to building an efficient geological map depending on the spectral signatures of each rock unit utilizing high spectral and spatial resolution sentinel 2 data (Shebl et al., 2022, 2021b) (Table 1). Moreover, and with the proven notability of machine learning algorithms in lithological mapping, support vector machine (SVM) was applied to build a predicted lithological map (Fig. 2).

The hydrogeologic setting is reported through the deep drilling tests for the oil and groundwater explorations and pointed out that, Sinai occupies six deep aquifers including Miocene, Eocene, Upper Cretaceous, Lower Cretaceous, Jurassic, and Paleozoic aquifer systems (EPIQ, 1998). Among these aquifers, the most important aquifers in Sinai is the Lower Cretaceous Nubian sandstone aquifer (Malha Formation) due to its wide extent, lithology, considerable storage and fairly good quality. In addition, these aquifers were classified into three main water bearing formations; the Precambrian basement (El-Shamy and El-Rayes, 1992); the Cretaceous aquifers and the Quaternary aquifer (Shalaby, 1997).

3. Materials and methods

3.1. Remote sensing

In the current study, Sentinel 2 data were utilized in lithological classification, calculating Normalized Difference Vegetation Index (NDVI) and Normalized Difference Moisture Index (NDMI) (Fig. 3). A cloud-free, S2A MSI as an L1C product was obtained. Sentinel 2 preprocessing included georeferencing, and radiometric correction using sen2cor processor in Sentinel Application Platform (SNAP). Moreover, A 10 m Land Use/Land Cover map (LU/LC) was prepared through the recent Global Land Cover Map (GLCM) released by Esri that depends also on Sentinel 2 data.

PALSAR data, with 12.5 m Pixel size were obtained and used for drainage network extraction (using SAGA and QGIS software), slope mapping and lineaments delineation. The 3-km Soil Moisture Active Passive data (SMAP/Sentinel-1 L2_SM_SP) (Mao et al., 2019) are utilized for mapping soil moisture. Rainfall data were provided by Prediction of Worldwide Energy Resources (POWER) NASA Project.

Several image processing techniques (e.g., principal component analysis, and independent component analysis) were applied to discriminate the lithological units, however false color composite (FCC) of 12/11/2 in RGB gives a reasonable identification for all the exposed targets. Thus, a reference geological map (10 m pixel

Table 1
Characteristics of Sentinel 2 data (Shebl et al., 2022).

Band (b)	Central wavelength (μm)	Pixel size (m)
1	0.443	60
2	0.490	10
3	0.560	10
4	0.665	10
5	0.704	20
6	0.740	20
7	0.782	20
8	0.842	10
8a	0.865	20
9	0.945	60
10	1.375	60
11	1.610	20
12	2.190	20

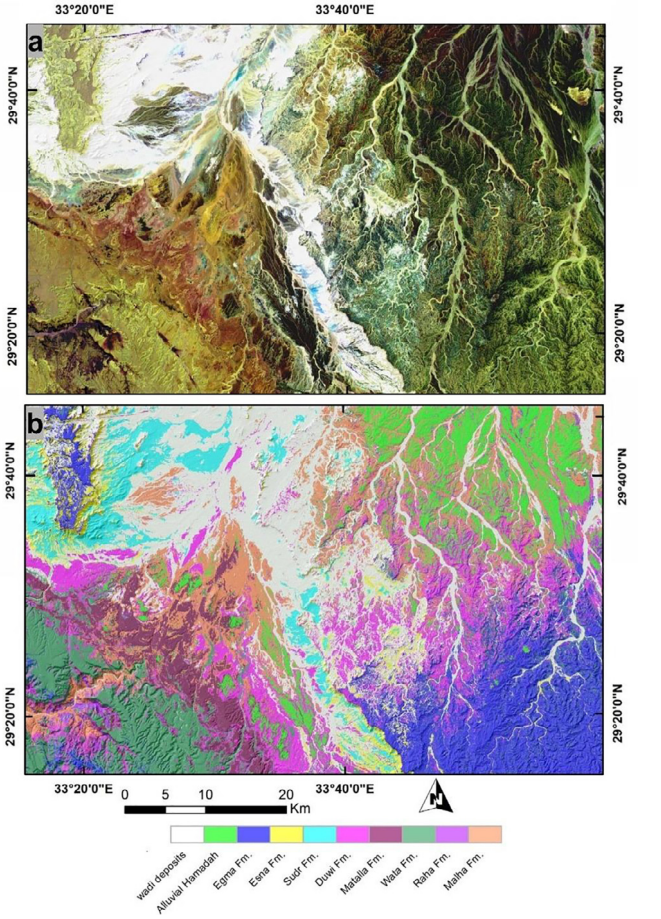

Fig. 2. a) FCC 12/11/2 RGB for lithological differentiation and b) lithological map of the study area created using SVM.

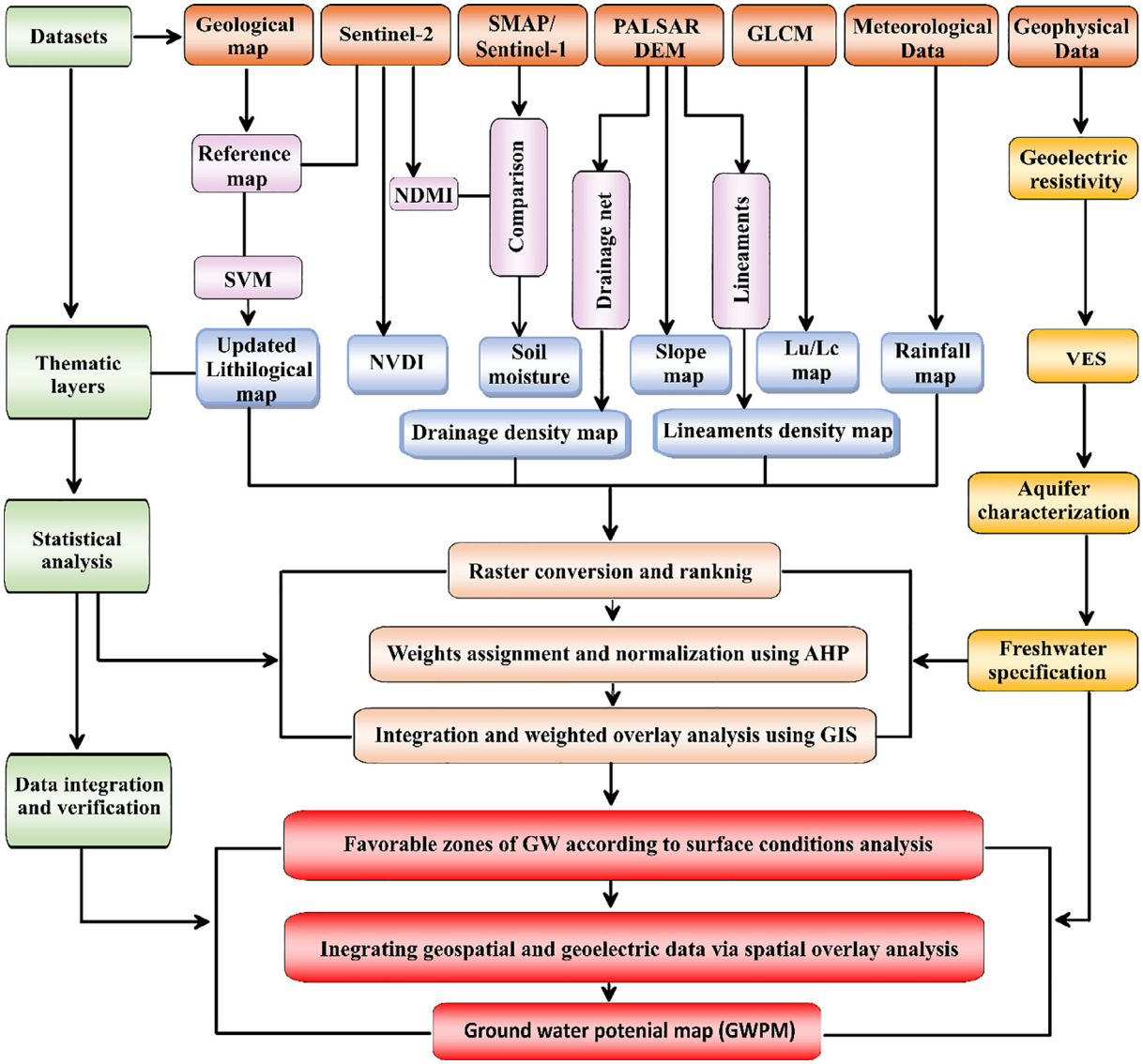

Fig. 3. Methodological Flow Chart.

size) was established via sentinel 2 FCC 12/11/2 in RGB respectively (Fig. 2a). This composite clearly sets apart all the exposed rock units after comparison with the georeferenced geological map. To avoid scale inconsistencies accompanied by the conventional geological map, this FCC was used for selecting training and testing samples for SVM classification (Table 2). The accuracy of the allocation process was assessed via confusion matrix (Appendix A), overall accuracy (88.6553%), and kappa coefficient (0.873), after testing the resultant lithologic map (Fig. 2b) with ground truth samples. Subsurface lithology (Fig. 4) could be interpreted through the measured resistivity data. The resistivity curves obtained by plotting the measured resistivity values against current electrode half spacing were first manually interpreted utilizing the standard and the generalized Cagniard graphs (KOEFOED, 1960) to construct an initial model exhibiting the thickness and resistivity for each layer. This initial model was then used to quantitatively interpret the various sounding curves using the IPI2WIN software developed by a scientific group in Moscow State University (IPI2WIN Program, 2010) with a Root Mean Square (RMS) error of less than 8 % for all VES points. To calibrate the interpreted resistivity models with the geological data from the boreholes, VES 9 was measured near the Jica 1 borehole (Fig. 1b) whose geological record is shown in Fig. 4 (JICA, 1992).

These eight parameters (Rainfall, Soil Moisture, NDVI, Lithology, Drainage Density, Lineament Density, Slope, and LU/LC) with different variables contribute to the process of highlighting ground water potentiality (GWP) in the study area (Fig. 3). Several methods are known for making a decision, e.g., simple additive weight

Table 2
Characteristics of training and testing data.

	Rock Unit	Training Pixels	Testing Pixels
1	Wadi Deposits (WD)	693	499
2	Alluvial Hamadah (AH)	700	458
3	Egma Fm (Eg)	777	482
4	Esna Fm (Es)	649	412
5	Sudr Fm (Su)	694	698
6	Duwi Fm (Du)	636	596
7	Matalla Fm (Mat)	734	622
8	Wata Fm (Wa)	774	602
9	Raha Fm (Ra)	537	526
10	Malha Fm (Mal)	677	385

Depth		Age	Lithology	Geological Description
From	To			
0	50	Paleocene		Wadi Deposits
50	180	Maastrichtian		Limestone intercalated with clay
180	270	Campanian		Claystone
270	385	Santonian-Coniacian		Limestone intercalated with clay
385	450	Turonian		Limestone
450	520			Chalky Limestone
520	585	Cenomanian		Limestone intercalated with clay
585	640			Limestone
640	670			Limestone intercalated with clay
670	700			Limestone
700	770			Limestone intercalated with clay
770	810			Limestone
810	865			Limestone intercalated with clay
865	1115	Lower Cretaceous		Alternation of shale and Sandstone
1115	1260	Jurassic		Sand and Shale

Fig. 4. Stratigraphic description of the Borehole JICA (JICA, 1992).

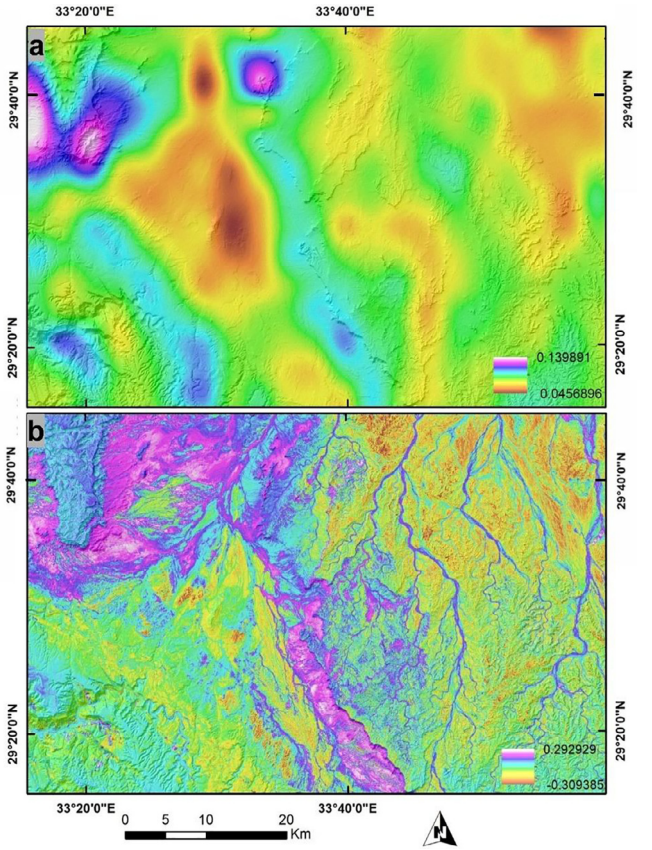

Fig. 5. Soil moisture maps using a) SMAP/Sentinel-1 data and b) Sentinel 2 Moisture Index (B8A-B11)/(B8A + B11).

Table 3
Normalized Eigenvector values of the analyzed elements.

Rank	Thematic Layers	Normalized Eigenvector (%)
1	Soil Moisture	28.7
2	Rainfall	24.2
3	Lithology	12.7
4	NDVI	11.3
5	Drainage Den	5.4
6	Lineament D	8.5
7	Slope	6.1
8	LULC	3.2

(Shebl et al., 2021a), Multi-influence factor techniques (MIF) (Das et al., 2017), and AHP. As an efficient multicriteria decision-making approach, AHP was recommended by several researchers (Nigussie et al., 2019; Panahi et al., 2017). Thus, AHP is adopted as a decision system for these shared parameters according to their relative influence to wisely classify the GWP of the study area, by assigning each pixel in the resultant thematic map a numerical value or weight reflecting its potentiality for fresh groundwater. The influence of each factor affecting GWP is controlled by comparative and intrinsic weights (Das et al., 2017). The former describes the relative importance between the main contributing factors, while the latter arranges the attributes of a single factor according to their importance for GWP. We used a pairwise comparison technique to give each criterion its weight based mainly on the full knowledge of the study area conditions and after consulting experts. The widely used scale (Wind and Saaty, 1980) makes the comparison much easier by giving a relative importance number ranging from 1 (equal importance) to 9 (extremely important) and a pairwise comparison matrix was established and the normalized principal eigenvectors were calculated for each criterion.

3.2. Electrical resistivity

The electrical resistivity approach is based on the measurement of electrical resistivity variations in the earth's subsoil. The concepts of electrical resistivity depend on the electrical direct current being injected via two electrodes known as current electrodes. Two more electrode pairs (potential electrodes) are used to measure the resultant potential difference. The apparent resistivity value (Milsom and Eriksen, 2013) can be then calculated as it follows:

$$\rho_a = K\frac{\Delta V}{I},$$

where ρ_a is the apparent resistivity in units of ohms/m, K is the geometric factor, ΔV is the potential difference, and I is the applied electric current.

For groundwater potentiality mapping, the Schlumberger array is employed using the electrical depth-sounding design to detect the vertical changes in electrical resistivity of the subsurface layers at higher depths (Chidambaram et al., 2013). In this configuration, all four electrodes are positioned in a line, with the outer electrode spacing being more than five times that of the inner electrode spacing. Only the current electrodes are moved during each measurement, while the potential electrodes remain in place, which are then moved when the signal becomes too weak. Through these procedures, the apparent resistivity values are subsequently obtained and interpreted to estimate the resistivity and thickness of each geoelectric layer (Sholichin and Prayogo, 2019).

To investigate the Lower Cretaceous Nubian sandstone aquifer (Malha Formation), seventeen deep vertical electrical soundings (VES) with current electrode half spacing AB/2 ranging from 5 to 3000 m were measured in the available valleys of the study area

as shown in Fig. 1b. The geoelectrical resistivity data measurements were carried out in the study area by using the SYSCAL R2 which was produced by IRIS instruments in France.

4. Results and discussion

4.1. Remote sensing results

The eight groundwater controlling elements were analyzed and classified according to the study area conditions, literature, and experts' opinion. Their normalized eigenvector values are shown in Table 3.

4.1.1. Soil moisture (SM)

Soil Moisture (SM) as the most potential variable in hydrogeology (Wang et al., 2020) got the first rank, as in this arid area moisture content strongly indicates the presence of groundwater, plants, or rainfall. Consequently, SM is mapped using 3-km SMAP (Mao et al., 2019), and Normalized Difference Moisture Index (NDMI) is calculated via the following equation (Gao, 1996; Taloor et al., 2021) utilizing Sentinel 2 Near Infrared (NIR) and Short-wave infrared (SWIR) bands:

$$NDMI = (NIR - SWIR1)/(NIR + SWIR1)$$

SMAP results and NDMI maps were compared, and a good correlation was found, where both of them highlighted the northwestern part of the study area with higher soil moisture, as shown in Fig. 5.

4.1.2. Rainfall

Rainfall is a main hydrological source for increasing groundwater storage (Arulbalaji et al., 2019) and directly impacts infiltration and storage depending on the nature of the slope and rock units exposed. The rainfall data were calculated for 15 points distributed within and just beyond the borders of the study area to help in building inverse distance weighted (IDW) rainfall interpolated map for the study area. IDW method was selected to create the continuous raster for the gauged points of rainfall as recommended by Nigussie et al. (2019). Our results revealed that the average winter rainfall of the study area ranges from 25.99 to 76.81 mm in 2016 as shown in the rainfall distribution map (Fig. 6a).

4.1.3. Lithology

Without suitable lithological conduits, rainfall cannot be easily infiltrated, and groundwater cannot be stored in aquifers. Thus, the third rank was preserved for lithology. The previously discussed thematic map (Fig. 2b) is adopted as the final geological map in this study. As an input for AHP, we reclassified the resultant geological map into 5 main divisions depending on their hydrogeological characteristics (mainly their permeability) as it follows: 1) very low (Sudr, Esna, and Egma Formations), 2) low (Raha, Wata, and Matalla Formations), 4) moderate (Duwi Formation), 5) high (Malha Formation), and 6) very high (alluvial hamadah and Quaternary wadi deposits).

4.1.4. NDVI

NDVI is considered a good indicator for groundwater especially in these regions and ecosystems. Thus, a pixel-based NDVI ranging from −1.0 to +1.0 is calculated in this study to assess GWP and to

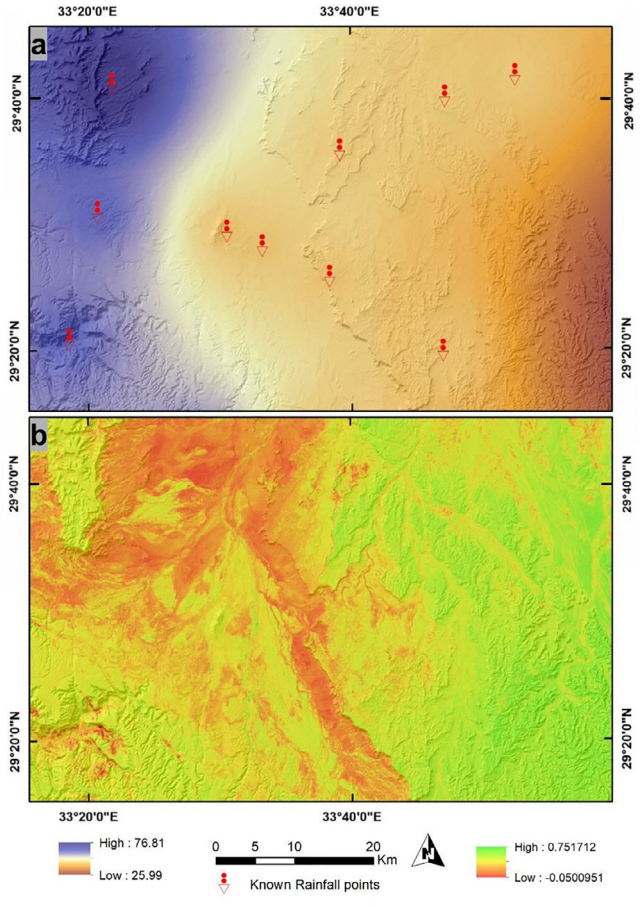

Fig. 6. a) Rainfall map in mm and b) Sentinel 2 normalized difference vegetation index (B8-B4)/(B8 + B4).

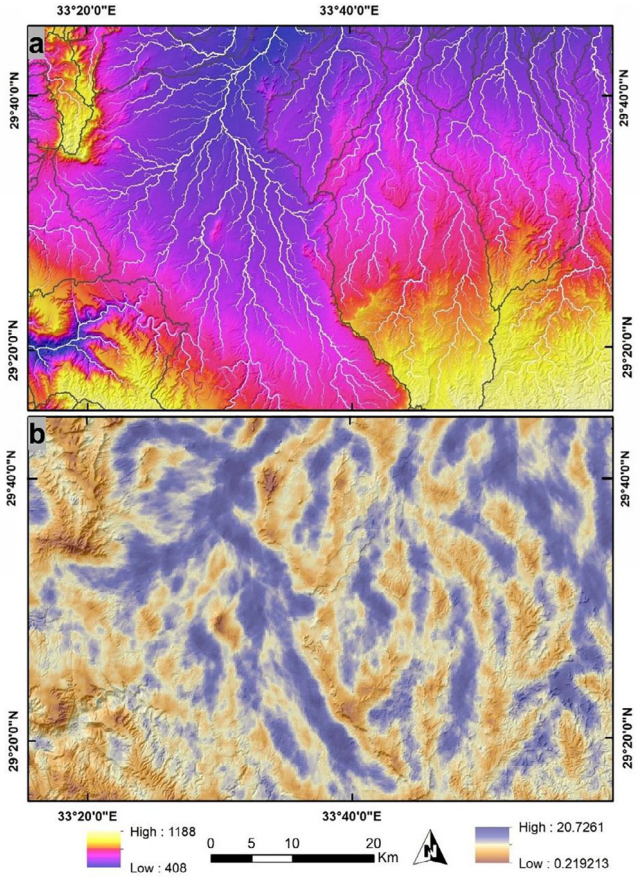

Fig. 7. a) Drainage network and sub-basins within the study area dropped over ALOS PALSAR DEM and b) Drainage Density map of the study area.

recognize the land covers in the study area by using the following equation (Taloor et al., 2021) applied to Sentinel 2 data:

$$NDVI = (NIR - Red)/(NIR + Red)$$

The resultant NDVI map values (Fig. 6b) range from −0.0500951 to 0.751712 and show scarce vegetation in the western side compared to the eastern part of the study area; however, scattered vegetation is represented all over the area.

4.1.5. Drainage network

The drainage network indicates the presence of rainfall and shows (together with slope) where the runoff water could be gathered. Ashmawy and co-workers compared in detail between the manually derived drainage network and those automatically extracted, and concluded the reasonable efficiency and reliability of the automated network in calculating morphometric parameters and achieving comprehensive watershed analysis (Ashmawy et al., 2018). The resultant automated network is displayed in Fig. 7a and shows high drainage densities (Fig. 7b) in the southeastern part of the study area resulting in higher runoff and lower GWP than the rest of the study area.

4.1.6. Lineament density

The presence of fractures is a good indicator for groundwater recharge, as these structural elements act mostly as pathways delivering surface water to the groundwater aquifers. Shebl and Csámer (2021) recommended PALSAR DEM in lineament extraction compared to the widely used optical datasets. Consequently, PALSAR DEM was implemented to derive lineaments, then, a lineament density map was created (Fig. 8a) to highlight zones of higher dissections that are favorable for groundwater infiltration.

4.1.7. Slope

Slope greatly affects runoff direction, groundwater recharge, and thus GWP. Areas with lower slopes (mostly flat) give more time for surface water to be infiltrated compared to steep or moderate slope (higher runoff) regions (Ibrahim-Bathis and Ahmed, 2016). The resultant slope map shows that gentle, moderate, and steep slopes are represented within the study area (slope ranges from 0° to 57.4°). Steep slopes are mainly associated with wadi cliffs at the central part of the study area or higher rock exposures at the western part; however, the northern central, and eastern parts are mostly flat regions, as shown in Fig. 8b.

4.1.8. LU/LC

Human activities have a profound impact on ecosystems, groundwater recharge, and quality (Scanlon et al., 2005). The constructed LU/LC map revealed that most of the study areas are scrubland or bare ground with a smaller representation of crops, built areas, and grass as shown in Fig. 9.

4.2. Geoelectric resistivity results

The results of data calibration between VES 9 and Jica 1 borehole showed the presence of four main geoelectrical units, as shown in Fig. 10. Above these geoelectrical units there is a geoelectrical layer (wadi deposits) separated into two subunits: the upper unit is the aerated near-surface unit with higher resistivity values than the lower unit, which is likely owing to wetness from surface infiltration and/or moistures. The first geoelectric unit represented by mostly Paleocene-Campanian clay with resistivity values between 4.41 and 11.9 Ω.m can be grouped into three stratigraphic units with a total depth of about 270 m. The second geoelectric unit is limestone with a resistivity of 117 Ω.m, which corresponds to three stratigraphic units from the Coniacian – Santonian to Turonian ages up to a depth of roughly 520 m. The third geoelectric

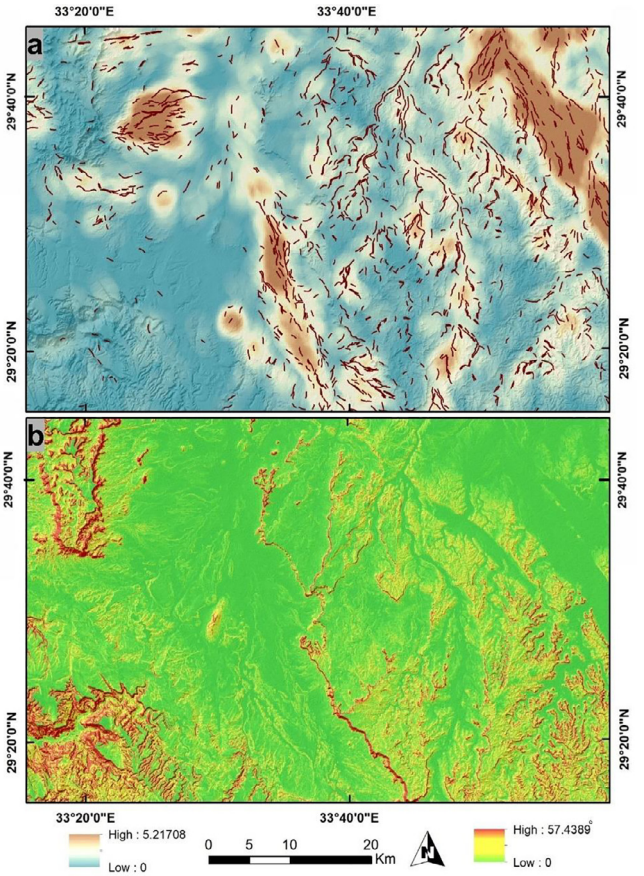

Fig. 8. a) Lineaments extracted from ALOS PALSAR DEM over their density map and b) Slop map in degrees of the study area.

unit extending to the depth of 865 m is built up of Cenomanian clayey limestone with a resistivity of 50.3 Ω.m. The fourth geoelectric unit is composed mainly of sandstone with a resistivity value of 412 Ω.m and represents the major aquifer of the Lower Cretaceous Nubian Sandstone deposits, which extend to a total depth of 1115 m.

4.2.1. Iso-resistivity maps

In the present study, iso-resistivity maps were constructed for each geoelectric unit using the interpreted true resistivities to

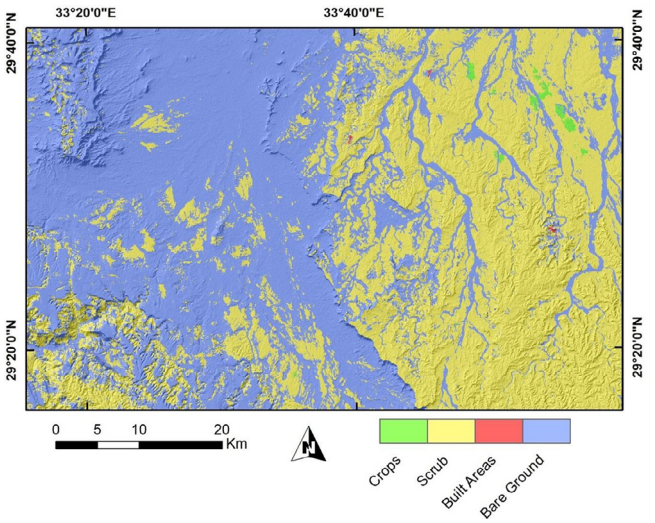

Fig. 9. a) Land use / land cover map of the study area.

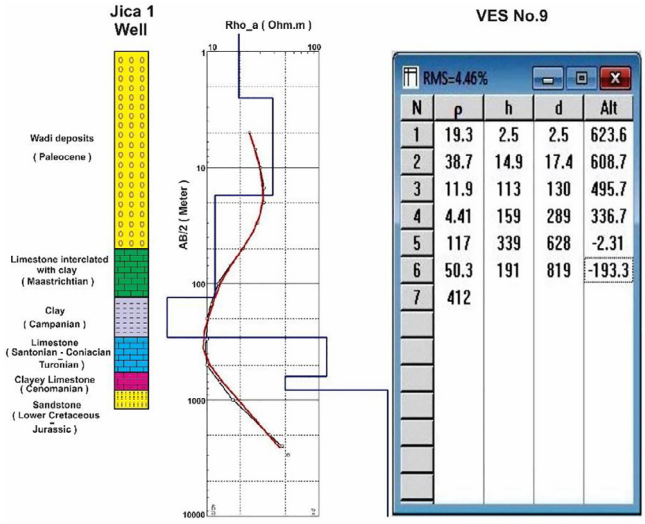

Fig. 10. Calibration between VES 9 and Jica 1 well.

illustrate the lateral variations in geoelectric resistivity values, as shown in Fig. 11. It is demonstrated that the first clay layer is characterized by relatively low resistivity values, ranging from roughly 3.1 Ω.m to 52 Ω.m. The minimal resistivities are extended in the central part from north to south at VES 9 and VES 8 as well as the southeastern part of the study area at VES 17,while, the maximum resistivity values are concentrated in the western and eastern parts of the study area at VES 2 and VES 16, respectively. Furthermore, the resistivity of the second geoelectric unit ranges from around 12.4 Ω.m to 230.1 Ω.m. The highest resistivity values are concentrated in the southwestern part at VES 4, the central north part at VES 9, and the eastern part at VES 15 and VES 16 while those of the lowest values are represented in the central part of the study area at VES 6, VES 7, VES 10, and VES 11 as well as the southeastern part at VES 17. Additionally, the third geoelectric unit has resistivities ranging from about 2.2 Ω.m to 57.6 Ω.m. The northwestern and northeastern parts including VES 10, VES 11, VES 14, VES 15, and VES 16 represent the lowest resistivity zone, whereas the highest values are concentrated in the southwestern part at VES 2 and VES 4 as well as the central north part at VES 9. Finally, the geoelectric resistivity contour map for the fourth unit representing the main aquifer of the Lower Cretaceous Nubian Sandstone has resistivity values ranging from about 57 Ω.m to 412.6 Ω.m. The lowest resistivity values are distributed over the northeastern part at VES 10, VES 11, VES 14, VES 15, VES 16, and VES 17, while those of the highest resistivities are demonstrated in the central-north part of the study area at VES 5, VES 6, and VES 9 and in the central-south part of a small extension at VES 8. The differences in resistivity levels are thought to be caused by the varied salinity rates of the groundwater that has saturated the aquifer, as evidenced by several studies (Abd El Rahman, 2001; Abd El Samie and Sadek, 2001; Basheer and Alezabawy, 2020; Ghoubachi, 2013; Shalaby et al., 2012). It means that this aquifer may contain good quality fresh groundwater in the western part and the salinity is increased towards the eastern part of the study area due to clay intercalation.

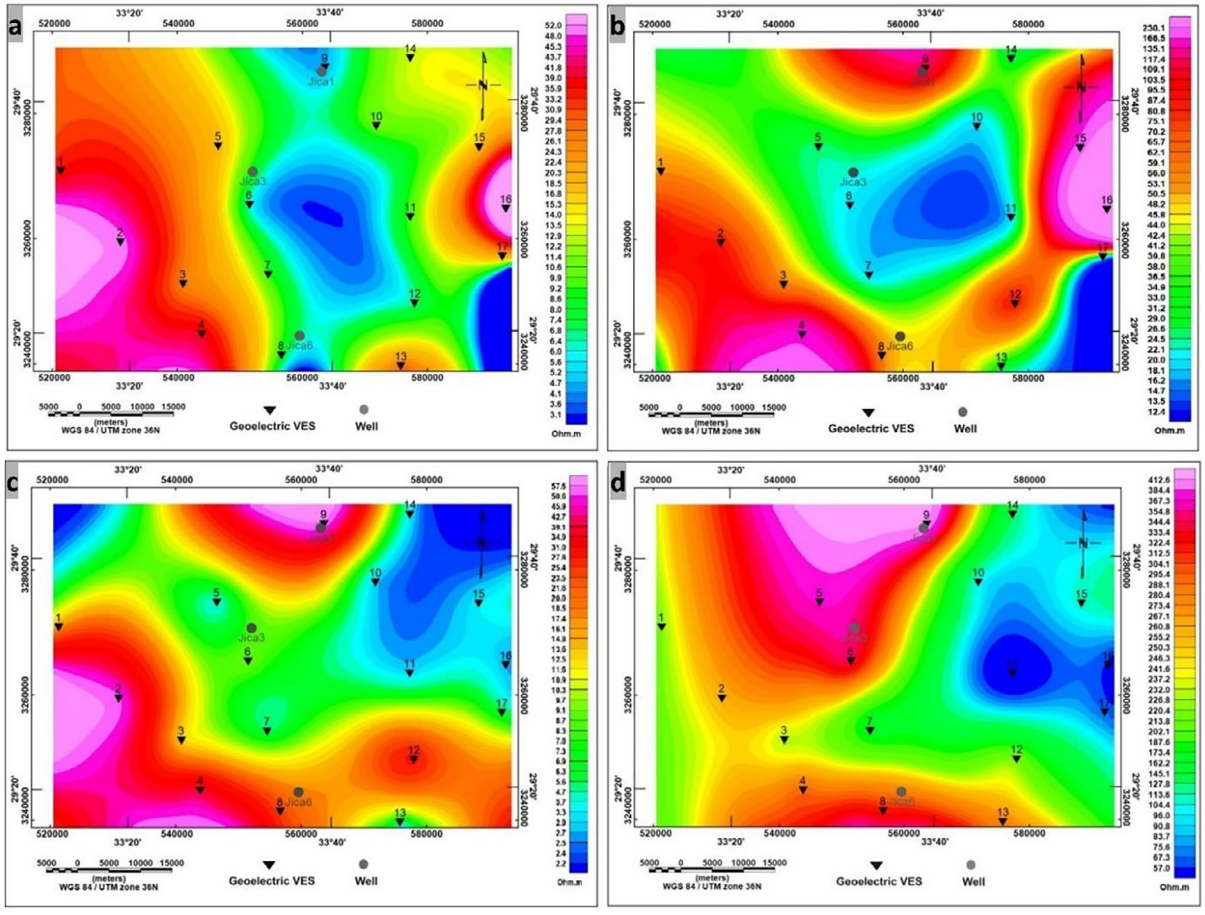

Fig. 11. Isoresistivity maps for a) the first geoelectric unit, b) the second geoelectric unit. c) The third geoelectric unit, d) the fourth geoelectric.

4.2.2. Geoelectric cross-sections

To provide a clear picture of the subsurface geological and structural conditions in the study area, geoelectric cross-sections along with five different profiles (P1, P2, P3, P4, and P5) were constructed. Fig. 1b shows the major directions of the geoelectrical profiles and related soundings for each profile.

Fig. 12a-e show the geoelectric cross-sections constructed for the mentioned profiles. The quantitative interpretation illustrates that the clay layer is characterized by low resistivity values ranging from 3.7 Ω.m at VES 10 to 50 Ω.m at VES 2, and its thickness varies from 38 m at VES 4 to 349 m at VES 12. The second geoelectric unit of limestone has resistivity values ranging from 14.2 Ω.m at VES 11

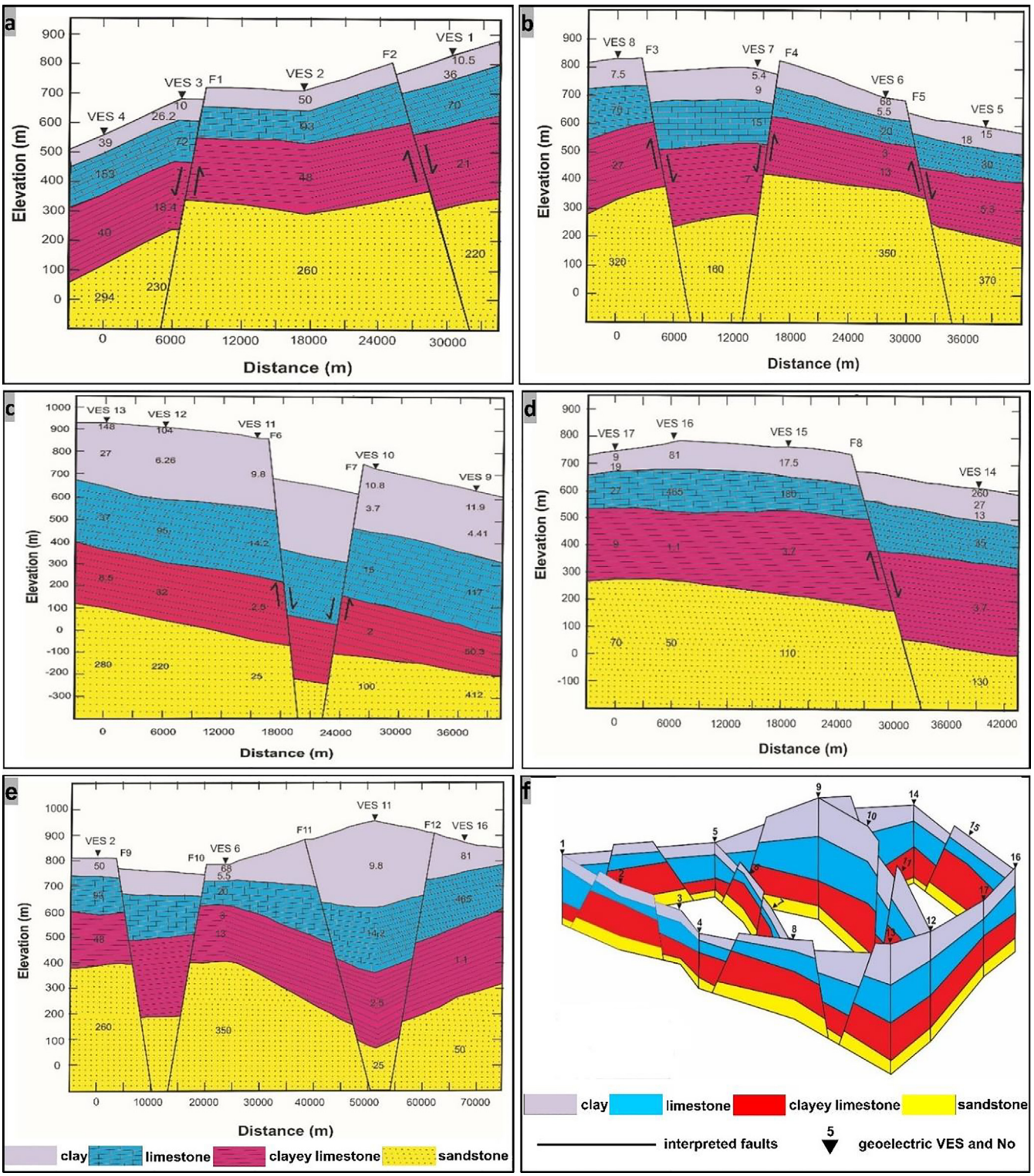

Fig. 12. Geoelectric cross-sections along a) profile P1, b) profile P2, c) profile P3, d) profile P4, e) profile P5, f) Panel diagram depicting a 3D view of the studied area's subsurface geological and structural pattern.

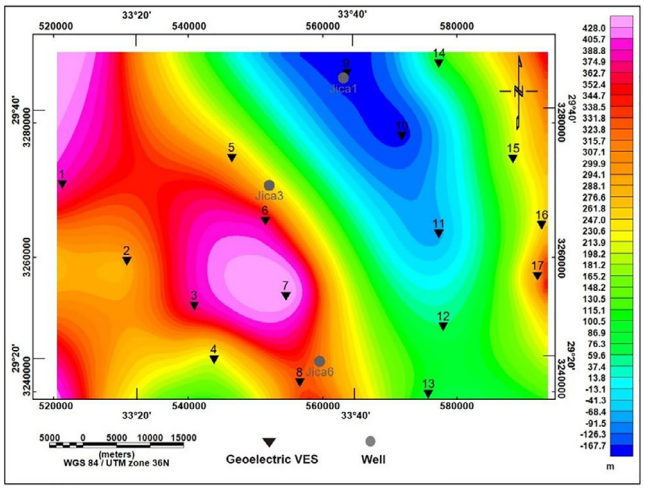

Fig. 13. Elevation contour map for the main aquifer in the study area.

to 465 Ω.m at VES 16, and its thickness varies from 35 m at VES 4 to 314 m at VES 10. The third geoelectric unit of clayey limestone has resistivity values ranging from 1.1 Ω.m at VES 16 to 50.3 Ω.m at VES 9, and its thickness varies from 150 m at VES 3 to 385 m at VES 14. The fourth geoelectric unit representing the Nubian sandstone aquifer of interest has resistivity values ranging from 25 Ω.m to 412 Ω.m at VES 11 and VES 9 respectively with unknown thickness due to its undetectable lower surface. Faults can be deduced to the different cross-sections based on lateral variation in lithology and resistivity readings. These faults are also confirmed by the surface mapped ones taking the trends of the Gulf of Aqaba, Gulf of Suez, and Syrian arc system.

A fence diagram (Fig. 12f) was produced along the first four main geoelectric profiles (P1, P2, P3, and P4) in the study area, as well as along the bordered soundings, showing the vertical and lateral changes in the subsurface geology.

4.2.3. Aquifer characterization

The water-bearing formation of the Lower Cretaceous Nubian sandstone aquifer represented by the fourth geoelectric unit receives great importance in this study. Fig. 13 shows the elevation contour map for the aquifer's top surface interpolated from the resistivity data of all VES points. The interpreted depth values for this aquifer range from about 316 m to 956 m below the surface. On the other hand, the aquifer has a minimum elevation from −168 m to −68 m relative to sea level at the central north part of the study area, while a zone with high elevation ranging from +375 to 428 m relative to sea level is represented in the western part with a NW-SE extension. We, therefore, can conclude that the upper surface of the aquifer decreases gradually towards the central and northeastern parts of the studied area suggesting the flow direction of the groundwater which coincided with the northern dip direction of Sinai's stratigraphic units (Shalaby et al., 2012).

5. Data integration and groundwater potentiality mapping

All the eight remote sensing criteria maps are reclassified into rasters with five classes (ranging from very low as 1 to very high as 5), as shown in Fig. 14 and Appendix B. Each reclassified map, with its appropriate weightage and known influence, is used as input to perform a spatial weighted overlay analysis to build a GWP map (Fig. 15a). The Consistency ratio (CR) value was 0.076, which indicates that the overall AHP is acceptable (i.e., CR < 0.1) (Nigussie et al., 2019). GWP map classifies the study area into five classes: (1) very low, (2) low, (3) moderate, (4) high, and (5) very high, occupying areas of 0.156, 1072.7, 2269.3, 367.1, 1.172 square kilometers respectively. Further inspection (depending on the topography and visual interpretation) of the resultant GWP map strongly highlights four main zones at the western part of the study area (A-D in Fig. 15a) with moderate to high and very high groundwater potentiality, recommended for drilling boreholes and groundwater extraction.

Geoelectrical results indicated that the differences in resistivity levels are thought to be caused by the varied salinity rates of the groundwater that has saturated the aquifer. It means that this aquifer may contain good quality fresh groundwater in the western part and the salinity is increased towards the eastern part of the study area due to clay intercalation. Spatial overlay analysis of geospatial and geoelectrical data highlighted the higher groundwater potentiality of the western part than the eastern side and revealed that three of these zones are approximately the same highlighted areas using electrical data results as shown in Fig. 15b. For instance, zone A in Fig. 15a almost totally coincides with zone A in Fig. 15b (pinkish and red colors indicate higher resistivity values, where there is a higher probability of freshwater existence compared to the lower resistivity blue zones that represent higher salinity groundwater). Thus, the integration could be concluded by delineating the highly potential freshwater zones using remote sensing and GIS results that depend mainly on rainfall with freshwater monitoring using geoelectrical resistivity results.

Verifying and coinciding with our outputs, spatial investigation of the known water wells within Sinai Peninsula (Elewa and Qaddah, 2011) revealed that 4 water points are mainly located in the western side of the study area (specified with higher fresh GW potentiality compared to the eastern side). Precise localization of the water wells revealed reasonable allocation with the GWPM (located within moderate to high potential groundwater zones) as shown in Fig. 15.

6. Conclusion

The current research manifests the effectiveness of implementing remote sensing and geoelectrical resistivity data in prospecting fresh groundwater in the western central part of Sinai. Soil moisture, rainfall, lithology, NDVI, drainage density, lineament density, slope, and LU/LC can be regarded as the primary groundwater controlling surface parameters. Using AHP these elements were combined and highlighted higher GWP at the western and central portions of the study area. The subsurface setting was inferred through 17 VESs that revealed the existence of four main geoelectrical units: (1) Paleocene to Campanian clay (11.9 Ω.m-4.41 Ω.m), (2) Coniacian – Santonian to Turonian limestone (117 Ω.m), (3) Cenomanian clayey limestone (50.3 Ω.m), and (4) Lower Cretaceous Nubian Sandstone (412 Ω.m). The latter represents the main aquifer in the study area. Iso-resistivity maps and geoelectric cross-sections highlighted the subsurface structural settings (exemplified through 3D view panel diagram) and suggested a flow direction towards the central and central northern parts of the investigated area in the major aquifers. Through iso-resistivity and elevation contour maps, three groundwater potential zones are highlighted. Through remote sensing and geoelectrical spatial data overlay, a strong correlation between the surface and subsurface investigations results was noticed in demonstrating the considered GWP of the western part and revealed that three zones (recommended for drilling groundwater wells) of the four (highlighted via remote sensing data) are approximately the same zones protruded by geoelectrical results. These results are rea-

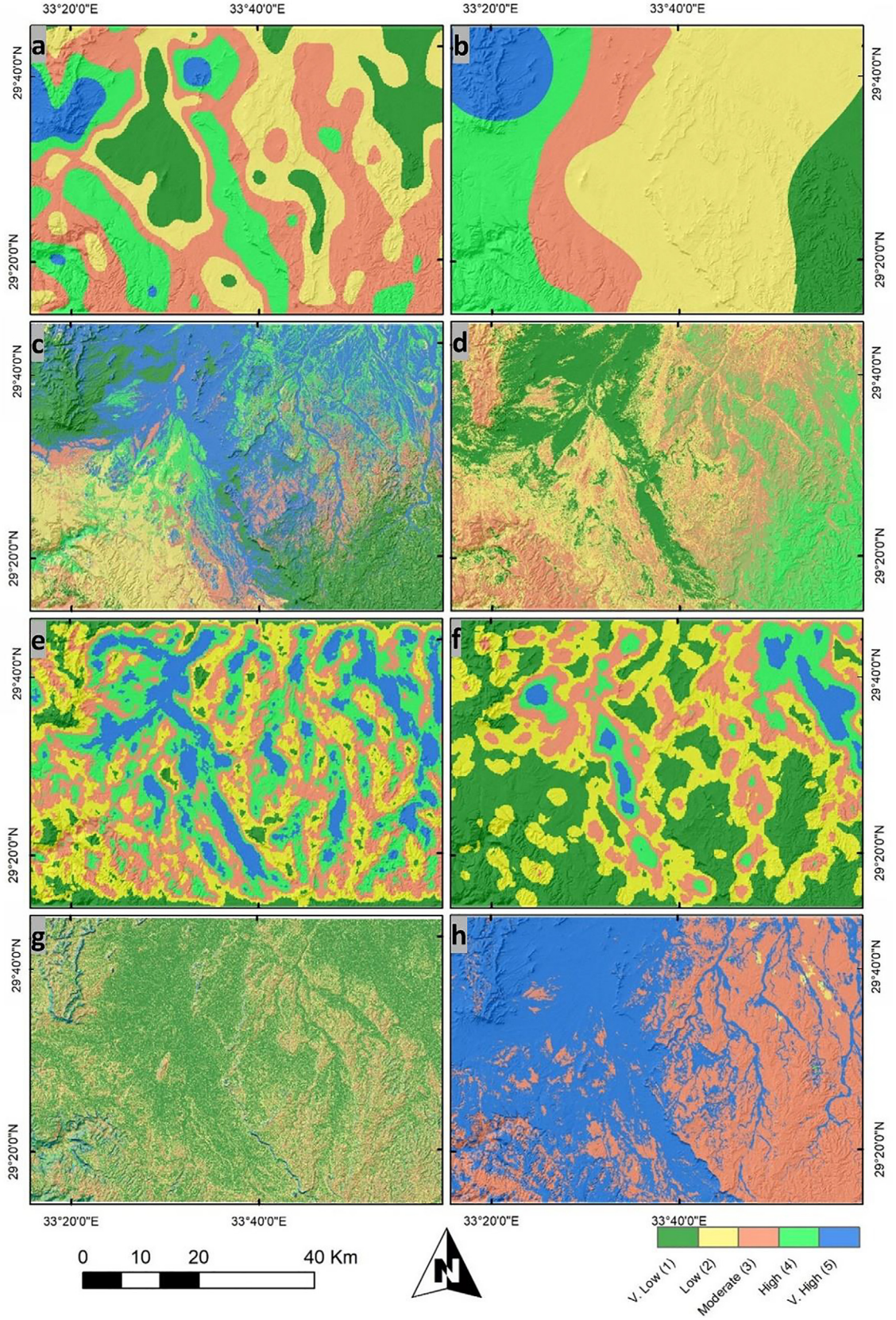

Fig. 14. Reclassified maps of a) Soil moisture, b) Rainfall, c) Lithology, d) NDVI, e) Drainage density, f) Lineament density, g) Slope and, h) LULC of the study area.

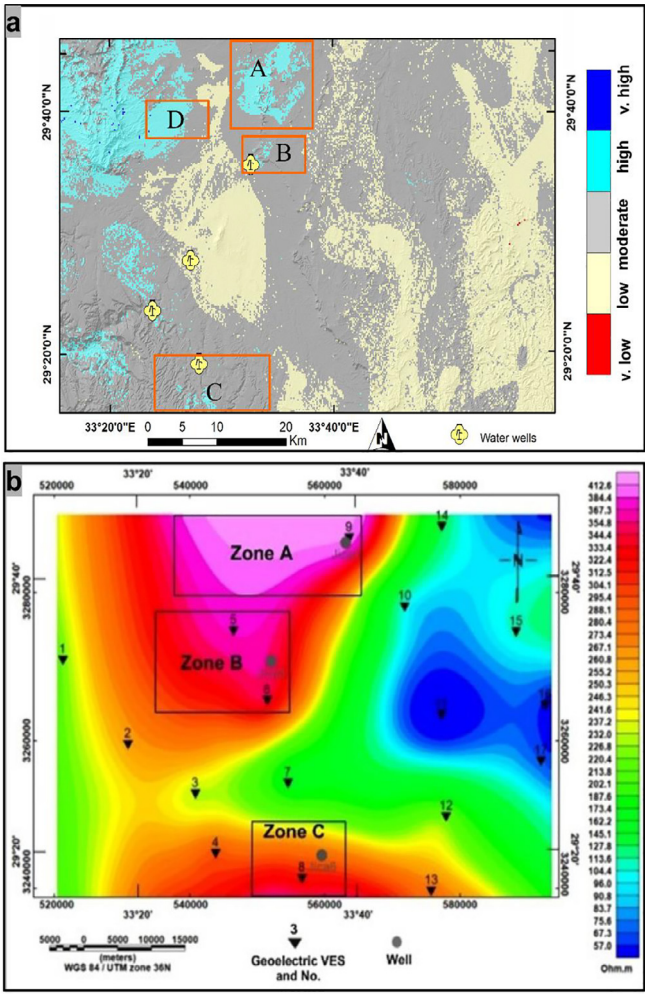

Fig. 15. a) GWPM constructed from 8 integrated remote sensing elements and highlighted 4 promising zones. b) Isoresistivity map for the aquifer showing approximately the same groundwater potential zones.

sonably verified through the spatial coincidence of 4 water wells within the western side of the study area. This, in turn, reflects the importance of remote sensing surface investigations in groundwater exploration programs. The applied integrated approach is strongly recommended for further groundwater prospecting as it helps at least in tapering the area to be surveyed by costly and time-consuming tools. Moreover, it could help decision-makers in sustainable groundwater management within the study area and its surrounding arid regions.

Funding

This research received no external funding.

Declaration of Competing Interest

The authors declare that they have no known competing financial interests or personal relationships that could have appeared to influence the work reported in this paper.

Acknowledgments

The authors would like to thank NRIAG, ESRI, NASA POWER, ASF, JAXA, and ESA for providing the data. Ali Shebl, Mahmoud Ibrahim Abdelaziz, and Mahmoud Abdellatif are funded by Stipendium Hungaricum scholarship under the joint executive program between Hungary and Egypt.

Appendix A. Error matrix, producer accuracy (PA), user accuracy (UA), overall accuracy (OA), and kappa coefficient (K) of SVM classification results.

S2	WD	AH	Eg	Es	Su	Du	Mat	Wa	Ra	Mal	Tot	PA (%)	UA (%)
WD	475	0	3	135	136	0	0	0	0	9	758	95.19	62.66
AH	0	458	0	0	0	0	0	0	1	0	459	100	99.78
Eg	0	0	453	0	0	0	0	8	0	0	461	93.98	98.26
Es	0	0	3	276	0	0	0	0	0	0	279	66.99	98.92
Su	9	0	0	1	562	0	0	0	0	0	572	80.52	98.25
Du	0	0	1	0	0	596	0	21	5	7	630	100	94.6
Mat	0	0	0	0	0	0	509	0	110	0	619	81.83	82.23
Wa	15	0	22	0	0	0	0	573	0	0	610	95.18	93.93
Ra	0	0	0	0	0	0	98	0	410	0	508	77.95	80.71
Mal	0	0	0	0	0	0	15	0	0	369	384	95.84	96.09
Tot	499	458	482	412	698	596	622	602	526	385	5280	OA=88.65	K=0.873

Appendix B. Score and weight assigned for the eight parameters.

Parameter	Class	Score	Weight
Soil Moisture	0.045–0.068	1	0.287
	0.068–0.079	2	
	0.079–0.090	3	
	0.090–0.108	4	
	0.108–0.139	5	
Rainfall (mm)	25.90–36.08	1	0.242
	36.08–46.26	2	
	46.26–56.44	3	
	56.44–66.62	4	
	66.62–76.79	5	
Lithology	Sudr, Esna, and Egma Formations	1	0.127
	Raha, Wata, and Matalla Formations	2	
	Duwi Formation	3	
	Malha Formation	4	
	alluvial hamadah and Quaternary wadi deposits	5	
NDVI	−0.050–0.050	1	0.113
	0.050–0.069	2	
	0.069–0.085	3	
	0.085–0.201	4	
	0.201–0.751	5	
Drainage Den.	0.2192–6.331	5	0.054
	6.331–9.065	4	
	9.065–11.55	3	
	11.55–14.29	2	
	14.29–20.72	1	
Lineament Den.	0.000–0.368	1	0.085
	0.368–0.920	2	
	0.920–1.739	3	
	1.739–2.946	4	
	2.946–5.217	5	
Slope (°)	0.000–3.378	5	0.061
	3.378–8.559	4	
	8.559–15.76	3	
	15.76–25.45	2	
	25.45–57.43	1	
LULC	crops	5	0.032
	scrub	3	
	bare ground	4	
	built areas	1	

References

Abd El Rahman, H., 2001. Evaluation of groundwater resources in lower cretaceous aquifer system in Sinai. Water Resour. Manag. 2001 153 15, 187–202. https://doi.org/10.1023/A:1013021008462.

Abd El Samie, S.G., Sadek, M.A., 2001. Groundwater recharge and flow in the Lower Cretaceous Nubian Sandstone aquifer in the Sinai Peninsula, using isotopic techniques and hydrochemistry. Hydrogeol. J. 2001 94 9, 378–389. https://doi.org/10.1007/S100400100140.

Abu El-Magd, S.A., Eldosouky, A.M., 2021. An improved approach for predicting the groundwater potentiality in the low desert lands; El-Marashda area, Northwest Qena City, Egypt. J. Afr. Earth Sci. 179, 104200. https://doi.org/10.1016/J.JAFREARSCI.2021.104200.

Araffa, S.A.S., Sabet, H.S., Gaweish, W.R., 2015. Integrated geophysical interpretation for delineating the structural elements and groundwater aquifers at central part of Sinai Peninsula, Egypt. J. African Earth Sci. 105, 93–106. https://doi.org/10.1016/J.JAFREARSCI.2015.02.011.

Arnous, M.O., El-Rayes, A.E., 2013. An integrated GIS and hydrochemical approach to assess groundwater contamination in West Ismailia area, Egypt. Arab. J. Geosci. 6, 2829–2842. https://doi.org/10.1007/S12517-012-0555-0/FIGURES/10.

Arnous, M.O., El-Rayes, A.E., Geriesh, M.H., Ghodeif, K.O., Al-Oshari, F.A., 2020. Groundwater potentiality mapping of tertiary volcanic aquifer in IBB basin, Yemen by using remote sensing and GIS tools. J. Coast. Conserv. 24, 1–20. https://doi.org/10.1007/S11852-020-00744-W/FIGURES/16.

Arulbalaji, P., Padmalal, D., Sreelash, K., 2019. GIS and AHP techniques based delineation of groundwater potential zones: a case study from Southern Western Ghats, India. Sci. Reports 2019 91 9, 1–17. https://doi.org/10.1038/s41598-019-38567-x.

Arunbose, S., Srinivas, Y., Rajkumar, S., Nair, N.C., Kaliraj, S., 2021. Remote sensing, GIS and AHP techniques based investigation of groundwater potential zones in the Karumeniyar river basin, Tamil Nadu, southern India. Groundw. Sustain. Dev. 14, 100586. https://doi.org/10.1016/J.GSD.2021.100586.

Ashmawy, M.H., Abd El-Wahed, M.A., Kamh, S.Z., Shebl, A., 2018. Comparative study of the drainage basin morphometry extracted from topographic maps and SRTM DEMs: an example from Ghadir watershed, Eastern Desert, Egypt. Sci. J. Basic Appl. Sci. 39, 52–64.

Basheer, A.A., Alezabawy, A.K., 2020. Geophysical and hydrogeochemical investigations of Nubian sandstone aquifer, South East Sinai, Egypt:

Evaluation of groundwater distribution and quality in arid region. J. African Earth Sci. 169,. https://doi.org/10.1016/J.JAFREARSCI.2020.103862 103862.
UNSECO Cairo Office, 2005. Geologic Map of Sinai, Egypt, Scale 1:500,000, project for the capacity building of the Egyptian geological survey and mining authority and the national authority for remote sensing and space science in cooperation with UNDP and UNSECO. Geological Survey.
Chidambaram, S. et al., 2013. Identification of groundwater potential zone by using GIS and electrical resistivity techniques in and around the Wellington reservoir, Cuddalore district, Tamilnadu, India. Eur. Sci. J., 9
Daniel Hervé, G., Kokea Ariane Darolle, F., Fidèle, K., David, Y., 2021. Groundwater prospecting using remote sensing and geoelectrical methods in the North Cameroon (Central Africa) metamorphic formations. Egypt. J. Remote Sens. Sp. Sci. https://doi.org/10.1016/J.EJRS.2021.10.003.
Das, S., Pardeshi, S.D., 2018. Integration of different influencing factors in GIS to delineate groundwater potential areas using IF and FR techniques: a study of Pravara basin, Maharashtra, India. Appl. Water Sci. 2018 87 8, 1–16. https://doi.org/10.1007/S13201-018-0848-X.
Das, S., Gupta, A., Ghosh, S., 2017. Exploring groundwater potential zones using MIF technique in semi-arid region: a case study of Hingoli district, Maharashtra. Spat. Inf. Res. 25, 749–756.
Elbarbary, S., Araffa, S.A.S., El-Shahat, A., Abdel Zaher, M., Khedher, K.M., 2021. Delineation of water potentiality areas at Wadi El-Arish, Sinai, Egypt, using hydrological and geophysical techniques. J. Afr. Earth Sci. 174,. https://doi.org/10.1016/J.JAFREARSCI.2020.104056 104056.
Elbeih, S.F., Madani, A.A., Hagage, M., 2021. Groundwater deterioration in Akhmim District, Upper Egypt: A Remote Sensing and GIS investigation approach, Egypt. J. Remote Sens. Sp. Sci. https://doi.org/10.1016/J.EJRS.2021.10.002.
Elewa, H.H., Qaddah, A.A., 2011. Groundwater potentiality mapping in the Sinai Peninsula, Egypt, using remote sensing and GIS-watershed-based modeling. Hydrogeol. J. 19, 613–628. https://doi.org/10.1007/S10040-011-0703-8/TABLES/6.
El-Rayes, A.E., Arnous, M.O., Al-Oshari, F., El-Rayes, A., Arnous, M., 2020. Integrated groundwater contamination assessment of tertiary volcanic aquifer, IBB Basin, Yemen, in: The 13 International Geological Conference (SSG 2020), Jeddah, Saudi Arabia. https://doi.org/10.13140/RG.2.2.26434.40643.
El-Shamy, I.Z., El-Rayes, A.E., 1992. Hydrogeologic assessment of Saint Catherine area, South Sinai, in: Proc. 3rd Conf. Geol. Sinai Develop., Suez Canal University, Ismailia, Egypt. pp. 71–76.
EPIQ, W.P.R.P., 1998. Hydrogeology of deep aquifers in the western desert and Sinai.
Fehri, R.M., 2021. A New Model Approach for Vulnerability to Assess Seawater Intrusion Risk for Monastir Aquifer System, Tunisia Related papers. https://doi.org/10.35840/2631-5033/1847.
Gao, B.C., 1996. NDWI—A normalized difference water index for remote sensing of vegetation liquid water from space. Remote Sens. Environ. 58, 257–266. https://doi.org/10.1016/S0034-4257(96)00067-3.
Ghoubachi, S.Y., 2013. Contribution to the hydrogeology of the Lower Cretaceous aquifer in east Central Sinai, Egypt. J. King Saud Univ. - Sci. 25, 91–105. https://doi.org/10.1016/J.JKSUS.2010.05.009.
Ibrahim-Bathis, K., Ahmed, S.A., 2016. Geospatial technology for delineating groundwater potential zones in Doddahalla watershed of Chitradurga district, India, Egypt. J. Remote Sens. Sp. Sci. 19, 223–234. https://doi.org/10.1016/J.EJRS.2016.06.002.
IPI2WIN Program, 2010. IPI2WIN Program. Version 3.1 2C; 17.10.08, 1990–2008. Copyright@1990-2010, Bobachev A.A., Programs set for VES data interpretation. Dep. Of Geophysics, Geological Faculty, Moscow State University, Russia, pp. 119899.
JICA, (JAPAN INTERNATIONAL COOPERATION AGENCY), North Sinai Groundwater Resources Study in the Arab Republic of Egypt 1992 Cairo, Egypt.
Koefoed, O., 1960. A generalized Cagniard graph for the interpretation of geoelectrical sounding data. Geophys. Prospect. 8, 459–469. https://doi.org/10.1111/J.1365-2478.1960.TB01728.X.
Kulandaisamy, P., Karthikeyan, S., Chockalingam, A., 2020. Use of GIS-AHP tools for potable groundwater potential zone investigations—a case study in Vairavanpatti rural area, Tamil Nadu, India. Arab. J. Geosci. 13, 1–15. https://doi.org/10.1007/S12517-020-05794-W/TABLES/12.
Kumar, M., Singh, P., Singh, P., 2022. Integrating GIS and remote sensing for delineation of groundwater potential zones in Bundelkhand Region, India, Egypt. J. Remote Sens. Sp. Sci. 25, 387–404. https://doi.org/10.1016/J.EJRS.2022.03.003.
Lee, S.C.H., Noh, K.A.M., Zakariah, M.N.A., 2021. High-resolution electrical resistivity tomography and seismic refraction for groundwater exploration in fracture hard rocks: A case study in Kanthan, Perak, Malaysia. J. Asian Earth Sci. 218, 104880. https://doi.org/10.1016/J.JSEAES.2021.104880.
Mao, H., Kathuria, D., Duffield, N., Mohanty, B.P., 2019. Gap filling of high-resolution soil moisture for SMAP/Sentinel-1: A two-layer machine learning-based framework. Water Resour. Res. 55, 6986–7009. https://doi.org/10.1029/2019WR024902.
Melese, T., Belay, T., 2021. Groundwater potential zone mapping using analytical hierarchy process and GIS in Muga Watershed, Abay Basin, Ethiopia. Glob. Challenges 2100068. https://doi.org/10.1002/GCH2.202100068.
Mills, A.C., Shata, A., 2009. Ground-water assessment of Sinai, Egypt. Groundwater 27, 793–801.
Milsom, J., Eriksen, A., 2013. Field geophysics, Fourth Edition Book review. Environ. Eng. Geosci. 19, 205–206. https://doi.org/10.2113/GSEEGEOSCI.19.2.205.
Mohamaden, M.I.I., Ehab, D., 2019. Application of electrical resistivity for groundwater exploration in Wadi Rahaba, Shalateen, Egypt. https://doi.org/10.1016/j.nrjag.2017.01.001 6, 201–209. https://doi.org/10.1016/J.NRJAG.2017.01.001.
Mukherjee, P., Singh, C.K., Mukherjee, S., 2012. Delineation of groundwater potential zones in Arid region of India—A remote sensing and GIS approach. Water Resour. Manag. 2012 269 26, 2643–2672. https://doi.org/10.1007/S11269-012-0038-9.
Naghibi, S.A., Pourghasemi, H.R., Pourtaghi, Z.S., Rezaei, A., 2015. Groundwater qanat potential mapping using frequency ratio and Shannon's entropy models in the Moghan watershed, Iran. Earth Sci. Inf. 8, 171–186. https://doi.org/10.1007/S12145-014-0145-7/TABLES/3.
Nigussie, W., Hailu, B.T., Azagegn, T., 2019. Mapping of groundwater potential zones using sentinel satellites (−1 SAR and -2A MSI) images and analytical hierarchy process in Ketar watershed, Main Ethiopian Rift. J. Afr. Earth Sci. 160, 103632. https://doi.org/10.1016/J.JAFREARSCI.2019.103632.
Ozdemir, A., 2011. GIS-based groundwater spring potential mapping in the Sultan Mountains (Konya, Turkey) using frequency ratio, weights of evidence and logistic regression methods and their comparison. J. Hydrol. 411, 290–308. https://doi.org/10.1016/J.JHYDROL.2011.10.010.
Panahi, M.R., Mousavi, S.M., Rahimzadegan, M., 2017. Delineation of groundwater potential zones using remote sensing, GIS, and AHP technique in Tehran–Karaj plain, Iran. Environ. Earth Sci. 76, 1–15. https://doi.org/10.1007/S12665-017-7126-3.
Qadir, J., Bhat, M.S., Alam, A., Rashid, I., 2020. Mapping groundwater potential zones using remote sensing and GIS approach in Jammu Himalaya, Jammu and Kashmir. GeoJournal 85, 487–504. https://doi.org/10.1007/S10708-019-09981-5/TABLES/10.
Riwayat, A.I., Nazri, M.A.A., Abidin, M.H.Z., 2018. Application of electrical resistivity method (ERM) in groundwater exploration. J. Phys. Conf. Ser. 995, 012094. https://doi.org/10.1088/1742-6596/995/1/012094.
Scanlon, B.R., Reedy, R.C., Stonestrom, D.A., Prudic, D.E., Dennehy, K.F., 2005. Impact of land use and land cover change on groundwater recharge and quality in the southwestern US. Glob. Chang. Biol. 11, 1577–1593. https://doi.org/10.1111/J.1365-2486.2005.01026.X.
Shalaby, A., Embaby, A., Seiam, A., 2012. Structural constraints on the groundwater regime of the Cretaceous aquifers in Central Sinai, Egypt. J. African Earth Sci. 75, 37–56. https://doi.org/10.1016/J.JAFREARSCI.2012.07.007.
Shalaby, A.I., 1997. Geomorphology and Hydrogeology of Wadi Watir basin, SE Sinai, Egypt. Thesis, Mansoura University, Egypt.
Shebl, A., Abdellatif, M., Hissen, M., Ibrahim Abdelaziz, M., Csámer, Á., 2021b. Lithological mapping enhancement by integrating Sentinel 2 and gamma-ray data utilizing support vector machine: A case study from Egypt. Int. J. Appl. Earth Obs. Geoinf. 105, 102619. https://doi.org/10.1016/J.JAG.2021.102619.
Shebl, A., Csámer, Á., 2021. Reappraisal of DEMs, Radar and optical datasets in lineaments extraction with emphasis on the spatial context. Remote Sens. Appl. Soc. Environ. 24, 100617. https://doi.org/10.1016/J.RSASE.2021.100617.
Shebl, A., Abdellatif, M., Elkhateeb, S.O., Csámer, Á., 2021a. Multisource data analysis for gold potentiality mapping of Atalla area and its environs, Central Eastern Desert, Egypt. Miner. 11, 641. https://doi.org/10.3390/MIN11060641.
Shebl, A., Kusky, T., Csámer, Á., 2022. Advanced land imager superiority in lithological classification utilizing machine learning algorithms. Arab. J. Geosci. 159(15), 1–13. https://doi.org/10.1007/S12517-022-09948-W.
Sholichin, M., Prayogo, T.B., 2019. Article ID: IJCIET_10_02_097 Cite this Article: Moh. Sholichin and Tri Budi Prayogo, Field identification of groundwater potential zone by VES method in South Malang. Int. J. Civ. Eng. Technol. 10, 999–1009.
Sultan, S., Mekhemer, H.M., M Santos, F.A., Abd Alla, M., 2009. Geophysical measurements for subsurface mapping and groundwater exploration at the central part of the Sinai peninsula, Egypt. Alla Arab. J. Sci. Eng. 34, 1.
Taloor, A.K., Manhas, D.S., Chandra Kothyari, G., 2021. Retrieval of land surface temperature, normalized difference moisture index, normalized difference water index of the Ravi basin using Landsat data. Appl. Comput. Geosci. 9,. https://doi.org/10.1016/J.ACAGS.2020.100051 100051.
Todd, D., Mays, L., 2004. Groundwater hydrology.
Wang, Q., Li, J., Jin, T., Chang, X., Zhu, Y., Li, Y., Sun, J., Li, D., 2020. Comparative analysis of Landsat-8, Sentinel-2, and GF-1 data for retrieving soil moisture over wheat farmlands. Remote Sens. 12, 2708. https://doi.org/10.3390/RS12172708.
Wind, Y., Saaty, T.L., 1980. Marketing Applications of the Analytic Hierarchy Process. http://dx.doi.org/10.1287/mnsc.26.7.641 26, 641–658. https://doi.org/10.1287/MNSC.26.7.641
Zarif, F., Isawi, H., Elshenawy, A., Eissa, M., 2021. Coupled geophysical and geochemical approach to detect the factors affecting the groundwater salinity in coastal aquifer at the area between Ras Sudr and Ras Matarma area, South Sinai, Egypt. Groundw. Sustain. Dev. 15,. https://doi.org/10.1016/J.GSD.2021.100662 100662.